AIAA JOURNAL
Vol. 38, No. 12, December 2000

Ultraviolet Radiation Modeling from High-Altitude Plumes and Comparison with Mir Data

S. F. Gimelshein* and D. A. Levin†
George Washington University, Washington, D.C. 20052
J. A. Drakes‡
Arnold Engineering Development Center, Arnold Air Force Base, Tennessee 37389-2213
G. F. Karabadzhak‡
TsNIIMASH, 141070, Korolev, Moscow Region, Russia
and
M. S. Ivanov§
Institute of Theoretical and Applied Mechanics, 630090, Novosibirsk, Russia

Modeling and calculations are presented with the goal of elucidating possible mechanisms of ultraviolet radiation from a Soyuz-TM spacecraft plume interacting with the ambient gas at altitudes of about 380 km, observed during the Mir experiment. The studies were performed with the direct simulation Monte Carlo method. The results presented include sensitivity studies of the simulations to various numerical parameters and an investigation of different radiation mechanisms. Among the mechanisms considered was the formation of OH(A) due to water dissociation by atomic O, collisional excitation of OH(X), and the formation of NH(A) by the reaction of atomic O with hydrazine fragments. The simulations are found to overpredict the data by approximately a factor of 5–70, depending on the parameters of the chemistry model chosen for water dissociation. However, the simulations are in close agreement with the near-field plume intensity profile.

I. Introduction

A PROGRAM to obtain calibrated high altitude plume imagery was initiated approximately one year ago. Using the Mir spacecraft as an observation platform, the program has been able to obtain radiance data from the ultraviolet (UV) to the visible spectral region on liquid propellant systems. The general concept of the experiment was to view the plumes of service spacecraft in low Earth orbit as they approach and leave the Mir station. Recent measurements of liquid propellant retrofirings with a UV imager have provided a new set of data worthy of analyses. The purpose of this paper is to present calculations that elucidate the significant radiation mechanisms in the flight regime corresponding to the newly obtained Mir experiment (MirEx) data.

Observations have been obtained from a number of missions between February 1998 and July 1999, with additional missions scheduled on the international space station. Of these missions, the 25 August 1998 Soyuz TK75 reentry firings results were of particular interest. The experimental arrangement, instrumentation, and the data have been discussed in detail in Ref. 1. At an altitude of about 380 km, 4 min of UV data of the Soyuz main engine (Progress) burn were obtained. The slant range from the Soyuz to the Mir varied from 15 to 30 km, thus ensuring good spatial resolution and high signal-to-noise ratio in the obtained imagery. The viewing geometry varied from 7 to 12 deg during the retrofiring. The data were acquired by a UV imager with a filter having a bandpass from approximately 270 to 310 nm. Radiometric calibration was performed with the aid of known UV stars. It was observed that the UV radiation was strong in the near field (within 30 m of the nozzle), weak in the plume far field (at a distance of about 1 km), and dependent on the orientation of the plume with respect to the velocity vector. Additional data obtained using the Soyuz attitude control system (ACS) thrusters during the 31 July 1998 mission showed similar radiation features. Both data sets, the Progress main engine (PME) and the Soyuz ACS, showed similar plume radiation. This suggests that chemical reactions of the specific propellant species with ambient atomic oxygen are important in determining the characteristics of the radiating plume.

One of the goals of the MirEx plume experiments is to identify the source of the UV plume radiation, which in turn requires identification of the dominant excitation mechanisms. Because the UDMH/N_2O_4 propellant produces large amounts of water (about 30% mole fraction), any electronically excited states produced by water dissociation, such as OH(A), are likely sources of radiation. Radiation from OH(A) has been examined by a number of authors for low-Earth-orbit conditions[2,3] and in higher density flight regimes.[4,5] The OH($A^2\Sigma^+ \rightarrow X^2\Pi$) radiation occurs at 310 nm, a wavelength within the optical bandpass of the UV imager. The paper will consider other possible sources of UV radiation, for example, collisional up-pumping of OH(X), trace amounts of propellant OH, and NH(A). The last has been shown to be a significant source of UV radiation for the shuttle primary reaction control system engines,[6] which has a propellant similar to that of Mir and its service spacecraft.

To predict the radiation distribution, the profile of species concentrations and temperatures in the plume is required. Because the plume images were obtained under conditions of highly rarefied, nonequilibrium flows, one must use a computational approach consistent with that of rarefied gas dynamics. The most powerful and promising approach for solving the Boltzmann equation is the direct simulation Monte Carlo (DSMC) method. Calculations will be compared with those performed earlier for the same conditions.[2] The paper discusses the sensitivity of the simulations to the computational domain size, cell size, and time step, all important factors in modeling the retrofiring plume, which exhibits large-density variations throughout the flow.

II. Numerical Method

To study strongly rarefied nonequilibrium flows, the widely used approach is the DSMC method,[7] which has become de facto the

Received 26 July 1999; revision received 7 February 2000; accepted for publication 28 April 2000.

*Research Scientist, Department of Chemistry; gimel@gwu.edu. Member AIAA.
†Research Professor, Department of Chemistry; dalevin@gwu.edu. Senior Member AIAA.
‡Research Scientist. Member AIAA.
§Head, Computational Aerodynamics Laboratory; ivanov@itam.nsc.ru. Senior Member AIAA.

main technique for studying complex multidimensional rarefied flows. The DSMC-based computational tool SMILE[8] is used in the computations presented here. An exact majorant frequency scheme for modeling collision process is utilized in SMILE. The time between consecutive collisions, τ, is simulated for each cell from the probability density $\nu_m \exp\{-\nu_m \tau\}$. Here, the majorant frequency of collisions ν_m is

$$\nu_m^l = [N_l(N_l - 1)/2][\sigma(v)v]_{\max}$$

where N_l is the number of molecules in the lth cell, $\sigma(v)$ is the total collision cross section, and v is the relative collision velocity. Different grids for collisions and macroparameters are used, which enables one to apply different adaption strategies. Both grids are two-level Cartesian grids adapted to flow gradients. Radial cell-based weights are employed to reduce significantly statistical scatter near the plume axis.

The retrofiring flow was computed as a steady axisymmetric flow. The sensitivity of the DSMC calculations to the number of cells and particles, as well as the size of the computational domain, will be discussed. The variable hard sphere model[9] was used for modeling molecular collisions, and the Larsen–Borgnakke model (see Ref. 10) with variable temperature-dependent rotational and vibrational relaxation numbers[11] was employed for energy transfer between translational and internal energy modes.

The total collision energy model[12] was used for modeling chemical reactions. In this model, an important parameter is the contribution of the internal, rotational and vibrational, energy modes of molecules to the reaction probability. The general form of the reaction probability for a dissociation or exchange reaction may be written as[12]

$$P_r(E_c) = a\frac{(E_c - E_r)^{b + X_c/2 + 1}}{E_c^{X_c/2 - 1}} \tag{1}$$

where E_r is the reaction threshold, a and b are constants dependent on the exponent in the variable hard sphere (VHS) model and the Arrhenius constants, and E_c and X_c are the energy and the number of degrees of freedom that contribute to reaction. E_c and X_c are assumed to be sums of relative translational, rotational, and vibrational terms,

$$E_c = E_{\text{trans}} + a_{\text{rot}}E_{\text{rot}} + a_{\text{vib}}E_{\text{vib}}$$

$$X_c = X_{\text{trans}} + a_{\text{rot}}X_{\text{rot}} + a_{\text{vib}}X_{\text{vib}}$$

where the parameters a_{rot} and a_{vib} determine the contribution of molecular rotations and vibrations to the reaction probability. Because chemical reaction cross sections are generally not available, a relationship between the reaction probability and the more readily available Arrhenius rate coefficient is required. As is explained in Ref. 12, the DSMC reaction probability (constants a and b) is derived from the reaction rate coefficient as

$$k(T) = AT^B \exp(-E_a/kT) \tag{2}$$

$$k(T) = \int_{E_a}^{\infty} P_r(E_c) f_e(E_c)\, \mathrm{d}E_c \tag{3}$$

where f_e is the equilibrium distribution function of E_c; also E_a, A, and B are the usual Arrhenius parameters, and E_r is set equal to E_a. Two limiting cases will be considered: $a_{\text{rot}} = a_{\text{vib}} = 0$ and $a_{\text{rot}} = a_{\text{vib}} = 1$.

III. Freestream Conditions and Experimental Setup

The typical altitude of the spacecraft during the observations ranged from 360 to 390 km. The freestream conditions used in this study correspond to an altitude of 380 km and are given in Table 1.

Because the flow at the nozzle exit is quite dense, a solution of the Navier–Stokes equations was used for a small region of the flow in the vicinity of the nozzle. The DSMC computation used the Navier–Stokes solution[2] obtained at the distance of 20 m downstream of the nozzle as the initial conditions. The profiles of the macroparameters of plume gas velocities and number density at 20 m, taken as the input for the DSMC method, are shown in Fig. 1. In Fig. 1, the abscissa is the distance perpendicular to the rocket-plume axis at 20 m from the nozzle. The mole fractions of the plume species are constant perpendicular to the flow and given in Table 2.

Table 1 Summary of freestream conditions

Property	Value
Temperature	883 K
Number density	1.34×10^{14} molecule/m^3
Soyuz-TM velocity	7350 m/s
O mole fraction	0.909
He mole fraction	0.0517
N_2 mole fraction	0.0393

Table 2 Species mole fractions 20 m downstream of the nozzle exit

Specie	Value
$X(H_2O)$	0.288
$X(N_2)$	0.267
$X(H_2)$	0.190
$X(CO)$	0.189
$X(CO_2)$	0.053
$X(H)$	0.013
$X(OH)$	1.07×10^{-5}

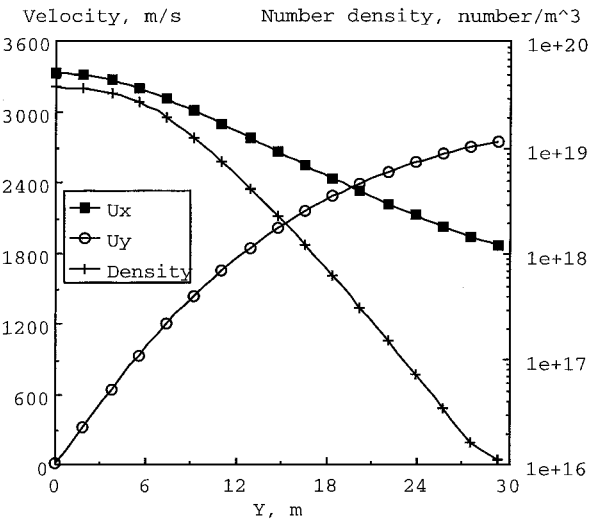

Fig. 1 Plume macroparameters at 20 m obtained by continuum approach, used as initial conditions for the DSMC calculations.

The modeling and calculations presented in this work are compared with the experimental data obtained on 25 August 1998. In this mission, the Soyuz-TM vehicle dedocked from Mir and drifted to a position 15 km behind Mir and 2 km above it. The Soyuz-TM motor was ignited at that position. During the retrofiring that lasted over 240 s, the Soyuz-TM decreased altitude from 385 to 375 km, and the view aspect angle increased from 7 to 14 deg (see Fig. 2). The plume filled the field of view during during the engine operation. To compare the modeling and experimental data, the radiation field was integrated through line of sights corresponding to the experimental view angle, with two more time-dependent factors also included. The first is the change in projected pixel size on the measured image, which scales as the square of the changing distance between Soyuz-TM and Mir, and the second is a slight change in the ambient gas density during the descent. All of these factors were included in calculation of the time-dependence radiance of the near field.

IV. Results and Discussion

A. Sensitivity to Parameters of the Approach

To calculate plume radiation at high altitudes with good accuracy, one needs to consider the choice of parameters for the computational approach, such as cell size, size of the computational domain, and time step. The sensitivity of the calculations to these simulation parameters is caused by both the high variation of density throughout

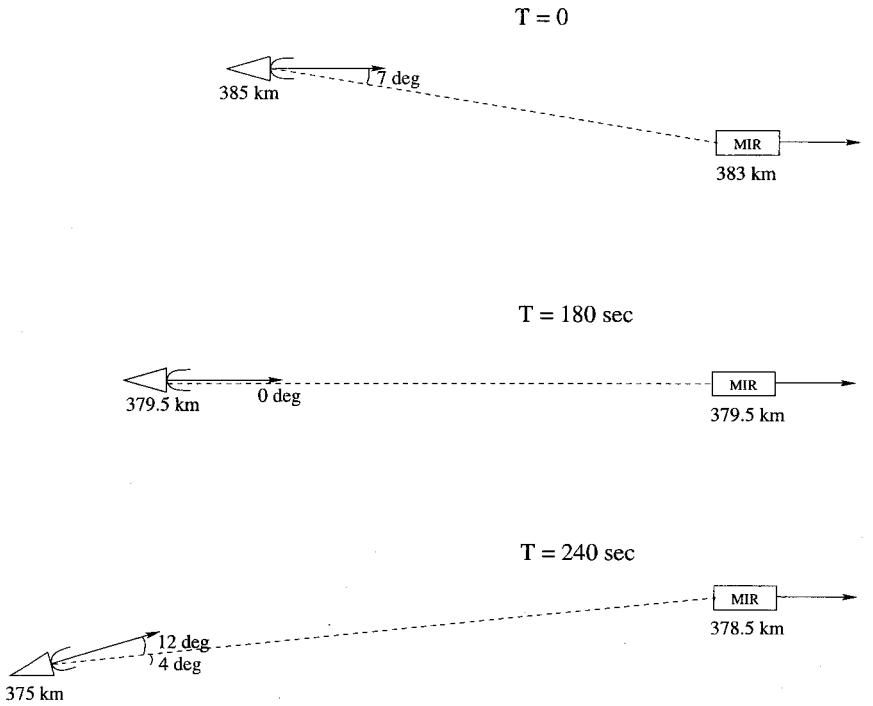

Fig. 2 Schematic showing Mir and Soyuz-TM orientation.

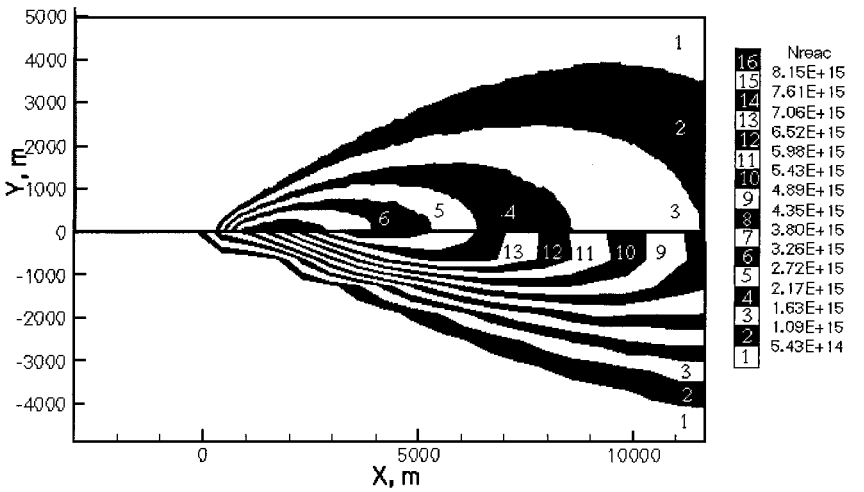

Fig. 3 Influence of grid resolution on the OH(A) radiance (upper field, adaptive grid, and lower field, 30 × 10 cells).

the flow and the large scales of the flow that expands over many kilometers away from the nozzle.

To test the sensitivity of the results to cell size, the computation was performed with an automatically adapted collision grid and with a nonadaptive Cartesian grid of 30 × 10 cells (the latter grid is similar to that used in Ref. 2). For the adaptive grid, the number of cells at steady state was about 75,000, and the adaption was performed based on the mean free path values. Very small cells with the linear size of the order of the local mean free path of 0.1 m were used near the plume starting surface, and large cells of 50 m were taken in the far field. The results were found to be quite different both in quality and quantity. Figure 3 shows the map of the number of radiative reactions $H_2O + O \rightarrow OH(A) + OH(X)$ per square meter per second (see legend) for the two grids. These values were obtained by the integration of the number of reactions per unit volume per unit time through the direction perpendicular to the plume axes. The radiance field is more extended in the plume direction for the coarser grid. The maximum value of radiation decreases by a factor of two with the grid refinement. The maximum values obtained on the coarse grid agree well with an earlier calculation.[2] Further computations with a nonadaptive collision grid of 300 × 100 showed a good agreement of the data with the results obtained on the adaptive grid. Note that these results were obtained on the computational domain of 15,000 × 5000 m and $a_{rot} = a_{vib} = 0$.

The computations were also performed for a larger domain of 23,000 × 5000 m to test sensitivity to computational domain size. In both cases, the nozzle was positioned at $X = 0$, and the left boundary was at $X = -3000$ m. The comparison of atomic oxygen velocities in X-axis direction (direction of the plume axis) is presented in Fig. 4. Figure 4 clearly shows that the velocity is essentially insensitive to the increase in size of the computational domain. There is only a negligible underprediction of the velocity values near the exit boundary for the smaller domain case (compared to the freestream velocity of 7350 m/s). It does not impact the radiation distribution because the maximum radiation is located at about 2000 m downstream of the nozzle exit.

The comparison of the numbers of radiative collisions along the centerline of the flow is given in Fig. 5 (compare open and closed circles) for two different computational domains: 15,000 × 5000 m and 23,000 × 5000 m. Note that the values presented were obtained through the integration of the radiation map through the lines of sight perpendicular to the plume axis. The number of radiative reactions

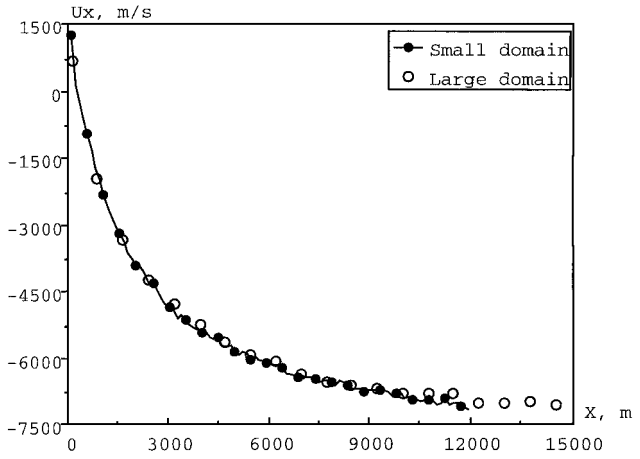

Fig. 4 Parallel velocity profiles along the plume axis for different computational domains.

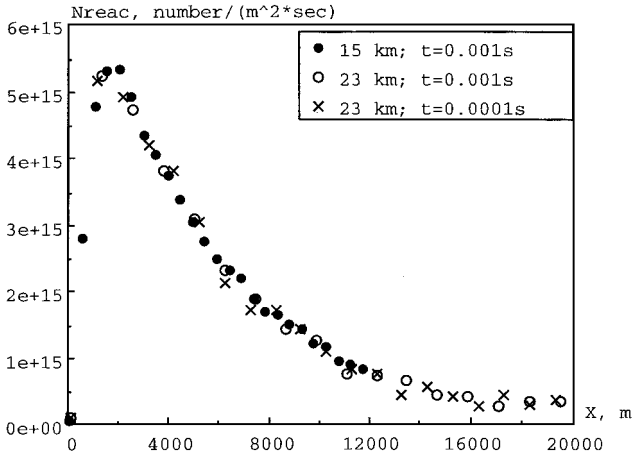

Fig. 5 Number of radiative reactions along the plume axis for different computational domains with the nozzle exit at $X = 0$, left boundary at $X = -3000$ m, and time steps.

for the larger domain and smaller time step is also presented in Fig. 5. The decrease of the time step by a factor of 10 does not change the results.

The last investigated parameter of the numerical method was the number of simulated particles in the computational domain. This number was varied from 90,000 to 300,000 molecules for the smaller computational domain. These changes did not affect the radiation map. As a result of these sensitivity studies, the optimal parameters were selected as follows. The computational domain is 15,000 × 5000 m, the number of simulated molecules is about 200,000, and the time step is 0.001 s. The collision grid was adaptive with the total number of cells about 70,000, and the macroparameter grid was a Cartesian grid with 300 × 100 cells.

B. Influence of the Chemistry Model

At this time, there are no data available that would enable one to assess the values of parameters of the chemistry model, a_{rot} and a_{vib}, for the most important reaction $H_2O + O \rightarrow OH(A) + OH(X)$. The problem is complicated significantly in the case of high-speed plume flows, where there is a strong nonequilibrium between the translational and internal molecular modes, and the translational energies are much higher than both rotational and vibrational ones. A reasonable assumption of $a_{\text{rot}} = a_{\text{vib}} = 0$ was made for this reaction in Ref. 2. However, the true contribution of molecular rotations and vibrations may be different from that. To study the influence of internal energy mode contribution, two opposite cases were considered, with $a_{\text{rot}} = a_{\text{vib}} = 0$ and $a_{\text{rot}} = a_{\text{vib}} = 1$. There is no contribution in the first case, and all internal modes of reacting molecules participate in reactions in the second case.

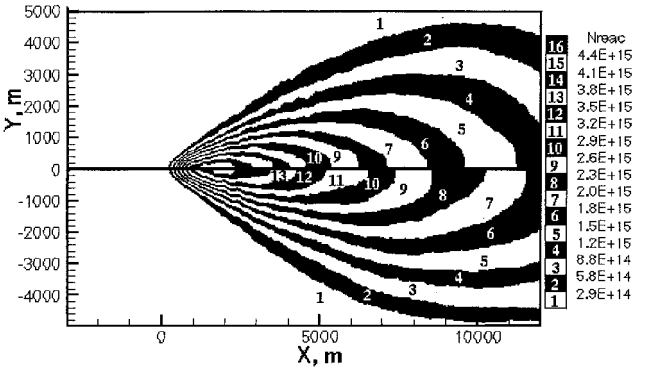

Fig. 6 Dependence of radiance contours on parameters a_{rot} and a_{vib} of the chemistry model: upper field, $a_{\text{rot}} = a_{\text{vib}} = 0$, and bottom field, $a_{\text{rot}} = a_{\text{vib}} = 1$.

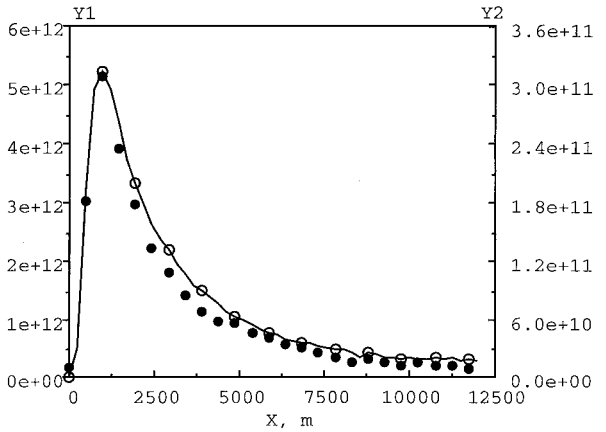

Fig. 7 Number of radiative reactions along the nozzle axis for different a_{rot} and a_{vib} per volume per time: closed circles, $a_{\text{rot}} = a_{\text{vib}} = 0$ (Y1 axis), and open circles, $a_{\text{rot}} = a_{\text{vib}} = 1$ (Y2 axis).

The computations showed that the magnitude of radiative emission is strongly dependent on a_{rot} and a_{vib}. The number of reactions per square meter per second (contour levels) obtained by $OH(A)$ production integrating through the plume perpendicular to the plume axis are shown in Fig. 6. The radiation is directly proportional to this value because the lifetime of the $OH(A)$ state is 6.9×10^{-7} s, which is orders of magnitude faster than the mean time between collisions (typically of the order of a second at 2 km downstream of the nozzle exit). Hence, quenching of $OH(A)$ in these flows is insignificant. The radiance values for $a_{\text{rot}} = a_{\text{vib}} = 1$ in Fig. 6 were multiplied by a factor of 15 for the sake of comparison. The general shape of the radiation spatial distribution is similar for the two cases. The inclusion of the internal energy modes slightly extends the radiative area in the plume axis direction; however, more important, it decreases the radiance approximately by a factor of 15. The number of reactions per volume per time unit is given in Fig. 7 for the two internal energy cases. The location of the radiation maximum is not changed for different a_{rot} and a_{vib}, but the magnitude of maximum is about 16 time less for $a_{\text{rot}} = a_{\text{vib}} = 1$, consistent with Fig. 6. Also, the falloff of the radiative emission downstream is slightly slower for this case.

The decrease in radiation with the inclusion of internal energy in the precollision parameters ($a_{\text{rot}} = a_{\text{vib}} = 1$) follows from Eq. (3). The general expression for $P_r(E_c)$ is dependent on a number of factors[9]; however, what is of interest is the ratio of P_r for the two limits,

$$\frac{P_r(a_{\text{rot}} = a_{\text{vib}} = 0)}{P_r(a_{\text{rot}} = a_{\text{vib}} = 1)} = \frac{\Gamma(2-\omega)}{\Gamma(2-\omega+\langle\zeta\rangle_1)} \cdot \frac{\Gamma(3/2+B+\langle\zeta\rangle_1)}{\Gamma(3/2+B)} \cdot \frac{(1-E_a/E_{c,0})^{1-\omega}}{(1-E_a/E_{c,1})^{1-\omega+\langle\zeta\rangle_1}} \cdot \left(\frac{E_{c,0}-E_a}{E_{c,1}-E_a}\right)^{B-\frac{1}{2}+\omega} \tag{4}$$

where ω is the temperature exponent of the coefficient of viscosity and is assumed equal to 0.25, B has the value of 1.3, the mean value of the internal number of degrees of freedom is $\langle\zeta\rangle_1 = (X_{\text{rot}} + X_{\text{vib}})/2$, $E_{c,0} = E_{\text{trans}}$, and $E_{c,0} = E_{\text{trans}} + E_{\text{rot}} + E_{\text{vib}}$. Because $E_{\text{trans}} \gg E_{\text{rot}} + E_{\text{vib}}$, the ratio of reaction probabilities can be further simplified to give

$$\frac{P_r(a_{\text{rot}} = a_{\text{vib}} = 0)}{P_r(a_{\text{rot}} = a_{\text{vib}} = 1)} \approx \frac{\Gamma(2-\omega)}{\Gamma(2-\omega+\langle\zeta\rangle_1)} \cdot \frac{\Gamma(3/2+B+\langle\zeta\rangle_1)}{\Gamma(3/2+B)} \cdot \left(\frac{1-E_a}{E_{\text{trans}}}\right)^{-\langle\zeta\rangle_1} \tag{5}$$

Substitution of a typical value for $\langle\zeta\rangle_1$ in the flow of about 1.5 and ω and B into Eq. (5) gives ratios on the order of 10–20, consistent with the results shown in Figs. 6 and 7.

The major conclusion of these results is that there is a need for more accurate reaction cross sections. Use of the total collision energy model leads to a large degree of uncertainty in the radiation modeling for highly nonequilibrium conditions.

C. Two Channels for Water Dissociation

Let us now consider in more detail the process of the formation of the OH species. There are two possible reaction paths for $H_2O + O$ interaction,

$$H_2O + O \rightarrow OH(A) + OH(X) \tag{6}$$

$$H_2O + O \rightarrow 2OH(X) \tag{7}$$

The two are interesting because the $OH(A)$ species is responsible for the UV radiation, whereas $OH(X)$ is a source of infrared (IR) radiation. Both mechanisms were considered in this work. To provide unbiased results, the reaction mechanisms (6) and (7) were included independently in two different calculations. In these computations, the assumption that $a_{\text{rot}} = a_{\text{vib}} = 0$ was used.

The value of the threshold for $OH(A)$ formation used in this work is taken from values given by Kofsky[13] and Baulch et al.[14] The expression for the rate (cubic meter per second) is given as,

$$k_{\text{KB}} = 3.8 \times 10^{-21} T^{1.3} \exp(-E_a/kT)$$

The activation energy E_a is essentially the sum of the change in standard enthalpy of the reaction (0.79 eV) and the energy to reach the $OH(A)$ excited electronic state of 4.01 to total 4.8 eV. The same preexponential of $3.8 \times 10^{-21} T^{1.3}$ was used for reactions (6) and (7), but an activation energy of $E_a = 0.79$ eV (Ref. 14) with no additional reaction barrier was used for the ground-state reaction.

The major factors that affect the reaction probabilities are the relative velocities of colliding H_2O and O and their density distributions. The density fields of these species are given in Fig. 8. It can be seen that the oxygen atoms do not penetrate close to the nozzle exit due to a sufficiently high density of the plume in that region. In contrast, the H_2O density is seen to decrease sharply with distance from the nozzle. Such density distributions cause the maximum of radiation to occur far downstream from the nozzle exit, where there are large enough densities of both H_2O and O.

The second factor that impacts the reaction probabilities is the relative velocity of H_2O and O. The H_2O velocity in the direction parallel to the plume axis (X direction) is shown in Fig. 9. The average water velocity changes slightly along the plume line (between 3100 and 3300 m/s). In general, the water-free stream oxygen atom relative collisional velocities are about 10,500 m/s, which corresponds to ~4.8 eV, a value close to reaction (6) threshold. In the outer portions of the flow, the H_2O velocity in the X direction is smaller, and as a result, the relative collision velocity in this portion of the flow is also smaller. Therefore, a smaller fraction of colliding particles has energy in excess of the energy threshold of reaction (6). The energy threshold of reaction (7) is much lower, and the area where these reactions may occur is, therefore, wider in the direction perpendicular to the plume axis.

These conclusions are shown in Figs. 10 and 11, where the number of reactions per volume per time unit is presented along the plume axis (Fig. 10) and in a cross section perpendicular to the plume axis, located at $X = 5000$ m (Fig. 11). The shape of the reaction number profiles along the plume axis is similar for the two reactions. The maximum is located at 1300 m downstream from the nozzle, and the number of reactions per unit volume per unit time for reaction (7) is larger approximately by a factor of 20. The profiles in the cross

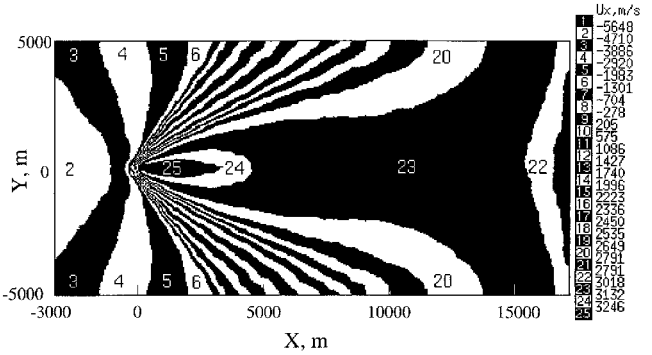

Fig. 9 Contour levels of H_2O velocity component parallel to the plume axis with a 20,000 × 5000 m computational domain.

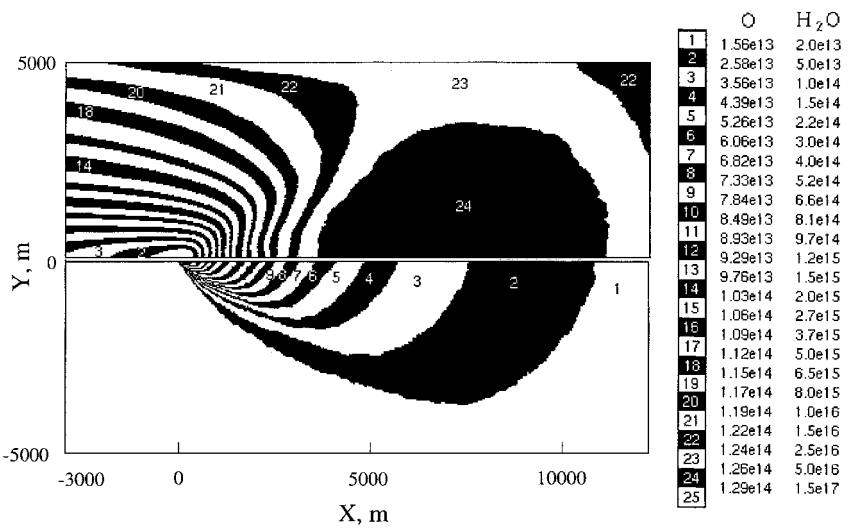

Fig. 8 Atomic oxygen (upper part) and water (lower part) number densities (the values in molecule per cubic meter) with a 15,000 × 5000 m computational domain.

section perpendicular to the nozzle axis also differ by approximately a factor of 20 at the periphery of the plume. The number of reactions per unit volume per unit time for reaction (7) decreases more gradually because particles colliding in the outer flow still have enough energy to overcome the small threshold for this reaction.

The possibility of OH(A) radiation through the collisional excitation of OH(X) molecules was also considered. Contour levels of OH(X) density and mean free path are presented in Fig. 12. The OH(X) number density is about two orders of magnitude smaller than that of H_2O in the region of high radiative emission, whereas its mean free path is about 2000 m (compare to about 150 m for H_2O). Also because the velocity of newly formed OH(X) molecules is relatively small compared to that of water, we can draw the conclusion that collisions resulting in OH(A) are not a significant source of radiation at the conditions under consideration. Note that a very small region of high OH(X) density near the nozzle exit is due to the presence of a small concentration of OH in the plume. The impact of plume OH molecules is negligibly small because their concentration throughout the flow is much smaller than OH molecules formed through reactions, except in the small vicinity of the nozzle.

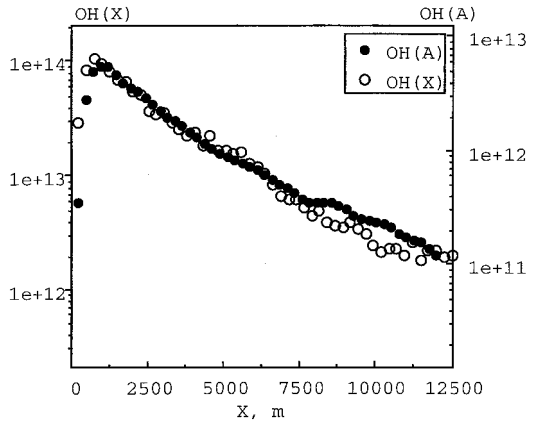

Fig. 10 Number of reactions (6) [OH(A)] and (7) [OH(X)] per cubic meter per second along the plume axis.

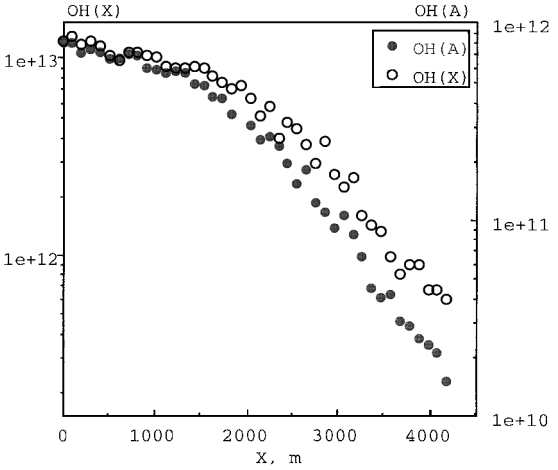

Fig. 11 Number of reactions (6) and (7) per cubic meter per second perpendicular to the nozzle axis at a distance of 5 km from the nozzle exit.

D. Potential Radiation from the NH(A) Electronically Excited State

In the results presented earlier, reaction (6) represents the sole source of UV radiation. Data exist, however, from the shuttle flight experiments of the shuttle primary reaction control system (PRCS) engines in a flight regime very similar to that of MirEx. The altitudes of the firings of the shuttle PRCS engines and the PME are 290–360 km vs approximately 370 km, both firing into essentially the same space environment. The propellants of both engines are similar. The PRCS uses a monomethyl hydrazine (MMH) instead of the UDMH propellant of the PME with the difference that the latter is doubly substituted with a methyl radical.

Given the similarity of the two experiments, we examined how our modeling could explore issues related to both sets of data. The presence of NH($A \rightarrow X$) 336-nm radiation was observed in the shuttle onboard GLO spectrograph.[6] Details about the experiment geometry, instrumentation, and postflight analyses of the data may be found in the work of Viereck et al.[6] Two GLO spectra are given[6] that show the presence of NH and OH. The absence of OH in one of the spectra may be due to the viewing geometry of the instrument. In general, the slices of the plume that were measured were close to the thruster (4 and 33 m downstream). The measurements, therefore, emphasize those regions close to the nozzle where the relative velocities will be lower. Had it been possible to obtain spectra farther downstream, OH might have been more prominent. Also ground-based IR measurements of the shuttle showed that OH(X) is observed, thus confirming at least the analog of the ground-state reaction.[3] The excited state product, OH(A), could not be measured with ground-based instruments due to atmospheric extinction.

Note that the optical passband wavelength dependence of MirEx is centered at the OH($A \rightarrow X$) transitions (310 nm), with the potential contribution from NH radiation reduced by one-fifth relative to that of OH ($A \rightarrow X$). The MirEx data, however, are broadband and cannot positively identify the spectral content of the radiation. Therefore, there are two data sets, neither one being totally complete. Moreover, it could be that the spectral content of the Mir images of the PME have two different spectral components. The near field could be dominated by radiation from NH(A) and the far field by OH(A).

To bridge the two sets of observations, the formation of NH(A) was added to the DSMC calculations. The work of Viereck et al.[6] did not specify the exact rate used in their DSMC calculations for NH

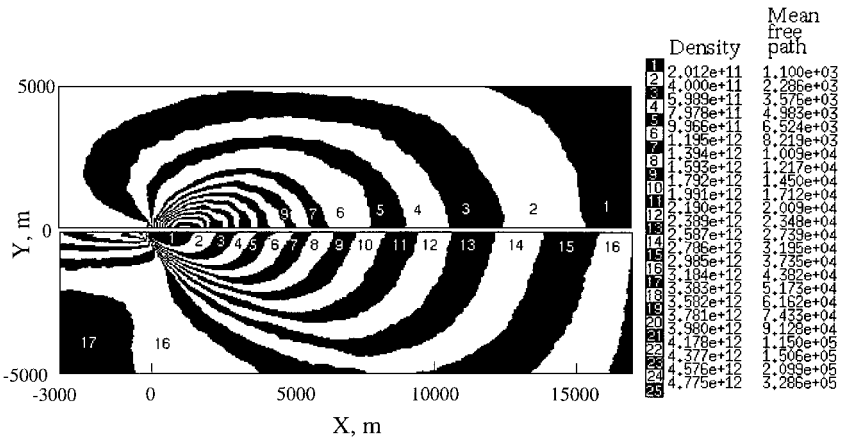

Fig. 12 OH(X) number density in molecule per cubic meter (upper field) and mean free path in meters (lower field); computational domain is 20,000 × 5000 m.

formation. A private communication with L. S. Bernstein verified that the rate (cubic meters per second) used was

$$k_{\text{frag}} = 2 \times 10^{-15} \exp(-29{,}000/T)$$

where the corresponding process is

$$\text{O} + \text{CH}_2\text{NH} \rightarrow \text{NH} + \text{H}_2\text{CO} \qquad (8)$$

It is postulated that NH is formed in the excited state due to the excess collision energy available, and similar to OH(A) formation, it is a single step process. The source of O is the freestream, and the source of CH_2NH is as an unburnt fragment of the propellant that has been suggested by other mass spectrometry measurements.[6] The threshold for the reaction is computed by using the ground-state thermodynamic enthalpy values for reactions (7) or (8) given in Table 2 of the work of Viereck et al.[6] corresponding to a change in enthalpy value ΔH of -1.20 eV. The activation energy for the excited state process, $E_a = 2.49$ eV, is computed by using the ground-state change in enthalpy value plus the additional 3.69 eV of energy to reach the A state of NH. The ΔH value for the decomposition of the hydrazine fragment is 2 eV lower in energy than for the formation of OH(X). For less energetic portions of the flow, that is, closer to the nozzle, this savings in energy could make the NH mechanism dominate. The choice of activation energy of 2.49 eV is consistent with the angular dependence of the shuttle GLO data (Bernstein, private communication). Because it is a one step process and because the source is a minor fragment of the propellant of unknown concentration, the preexponential factor (2×10^{-15}) times the initial fragment concentration is a free parameter. Bernstein (private communication) found an initial fragment mole fraction of 3×10^{-5} to be consistent with the data. Other work[15] cites a value of about 2×10^{-17} m^3 molecule^{-1} s^{-1} for the preexponential factor. In our calculations, we use the expression for k_{frag} and an initial mole fraction of 10^{-5}.

The values of $a_{\text{rot}} = a_{\text{vib}} = 0$ were assumed for both radiative reactions (6) and (7). The radiation contours for the two processes are given in Fig. 13 for a crossing geometry (aspect angle of 90 deg). To compare the predicted shape of the distributions, both sets of calculations were self-normalized. Figure 13 shows that there is a strong difference in the predicted shape of the two radiation sources. The higher reaction threshold for reaction (6) results in a spatial distribution more extended in the direction along the nozzle axis. Moreover, the maximum of the NH(A) radiation is observed to be significantly closer to the nozzle with wider radial spread than that of OH(A). The higher preexponential factor of reaction (8) has the effect of shifting the maximum radiation closer to the nozzle. This is clearly seen in Fig. 14, where the number of reactions per unit area per unit time for each mechanism is presented along the nozzle axis. The integrated values are given here to compare absolute values of radiation when looking through the glow.

Our calculations were performed assuming that the hydrazine fragment, CH_2NH, is present in concentrations of 0.001%. This gave a radiation value for NH(A) about two orders of magnitude smaller than for OH(A). If a larger concentration of hydrazine fragments were assumed, for example, 0.05%, the radiation emission due to reaction (8) would then become comparable to that of OH(A).

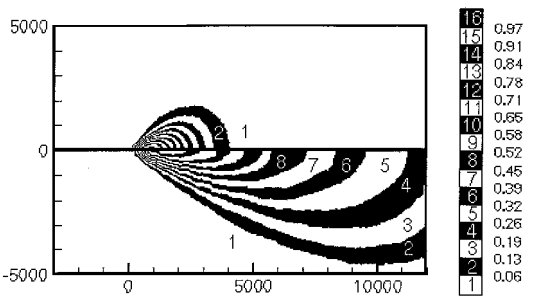

Fig. 13 Comparison of normalized radiance from NH(A) (upper field) and OH(A) (lower field).

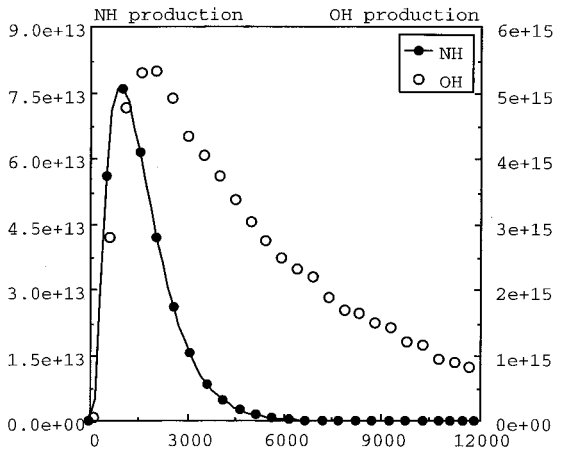

Fig. 14 Number of reactions (6) and (8) along the nozzle axis (number per square meter per second).

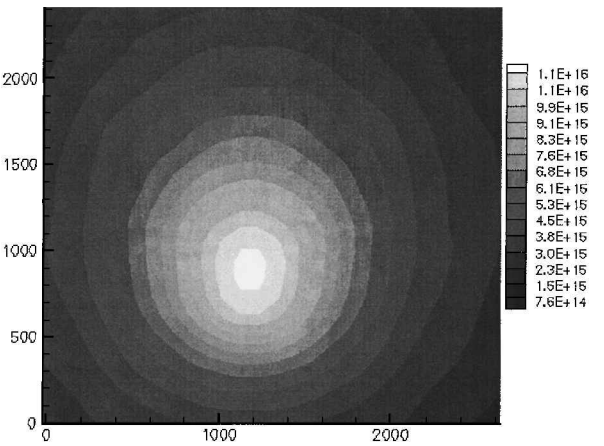

Fig. 15 Calculated OH(A) radiation contours (photons per square meter per second).

Imagery was obtained from a data collection in February 1999 of an identical PME firing. In contrast to the August 1998 data, however, portions of the data were taken with a bandpass filter centered at 310 nm. Examination of the February data showed that when the filter was used the signal decreased in proportion to the filter peak transmission (~17%). Hence, if the prominent source of radiation had been NH, instead of OH, the observed decrease would have been closer to the transmission of the filter at 336 nm, or 4%. Additional data collections are required to further address this question.

E. Comparison with Experimental Data

The results presented in the preceding sections showed radiation maps at a viewing angle of 90 deg, that is, perpendicular to the nozzle axis. The experimental data of 25 August 1998 were obtained for the thrust–wind angle changing from 174 to 167 deg [or aspect angle changing between 6 and 12 deg (see Fig. 2)]. To obtain data consistent with the experimental setup, the integration was performed for the angles corresponding to the experimental conditions. The comparison of computed and experimental radiation emission maps is given in Figs. 15 and 16. The calculated field was obtained through the integration of number of radiative reactions through parallel lines of sight. The image data[2] acquired at the Mir station at the start of the Soyuz-TM reentry burn filled the 8-deg field of view of the telescope, at a range from the Mir of 15 km.

The experimental image (Fig. 16) has been enhanced so that the bright region of the near field is saturated, whereas the far-field region of the plume is evident across the active portion of the image. The simulated image (Fig. 15) is presented in the core of the flow to have comparable dimensions with the experimental image, with a uniform scale used for the computed radiance. Note that the simulated image is presented for OH(A) radiation, which is presumed

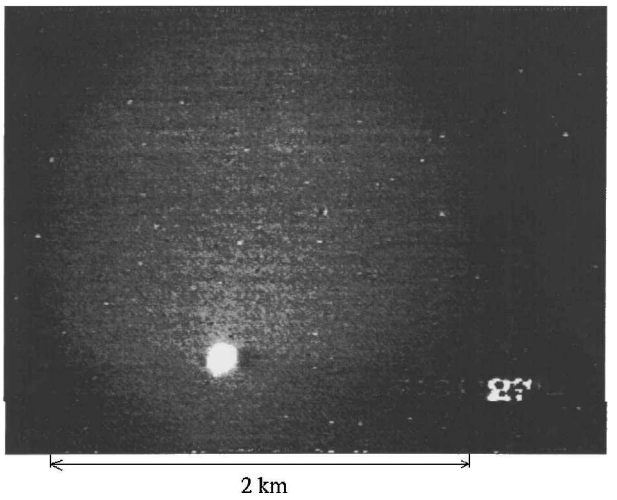

Fig. 16 Experimental radiation intensity.

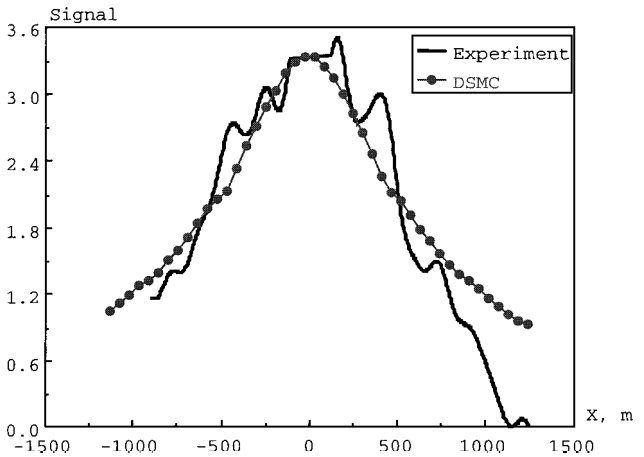

Fig. 17 Profiles of computed and measured radiances in the cross section passing through the brightest area of the flow.

to be the main source of the glow. Figure 17 shows a comparison of the experimental and computed radiances for a profile taken along a line parallel to the horizontal axis of Fig. 16 through the brightest region. The values are presented in arbitrary units, and near-field pixels are not included in the experimental profile because they have a much larger intensity associated with nozzle glow effects not related directly to this study. The agreement is quite satisfactory, especially in the region up to 1000 m. To provide a quantitative comparison with the measurements, a spatial integration was performed in the area of 2 km in diameter with the center located at the nozzle center. The corresponding total emission value observed in the experiment was approximately 3×10^{20} photon/s. The value calculated with $a_{\text{rot}} = a_{\text{vib}} = 0$ is 2×10^{22} photon/s, which overpredicts the experimental data by a factor of 70. For case $a_{\text{rot}} = a_{\text{vib}} = 1$, the value of radiation emission is about 1.6×10^{21} photon/s, which is much closer to the measurements but still overpredicts the data.

An interesting aspect considered in Ref. 1 is the measurement of the induction time demonstrated by the far-field plume at ignition. Whereas the near-field radiation shows an immediate rise after ignition, the induction time for the far field is about 2 s. This is clearly seen from Fig. 18, where the measured normalized intensity of the far field is shown as a function of time. One of the possible reasons for the induction could be an unsteady character of the plume during the first 2 s. Because one of the most transparent criteria (necessary but not sufficient) for a DSMC flow computation reaching steady state is the number of particles in the domain reaching a steady-state value, the number of particles in the far field was calculated as a function of time. The profile of the computed normalized number of particles is also shown in Fig. 18. A good agreement between

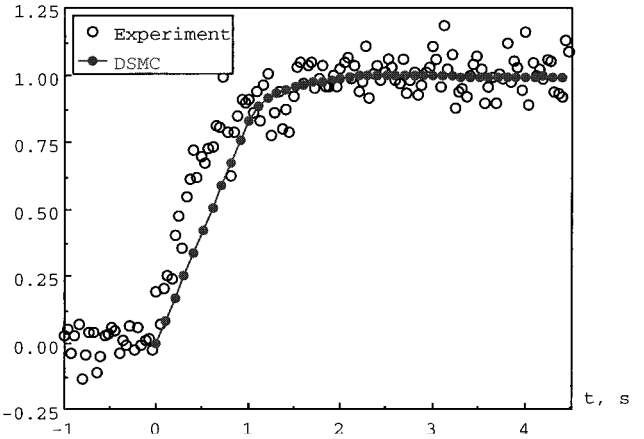

Fig. 18 Induction time for far-field plume.

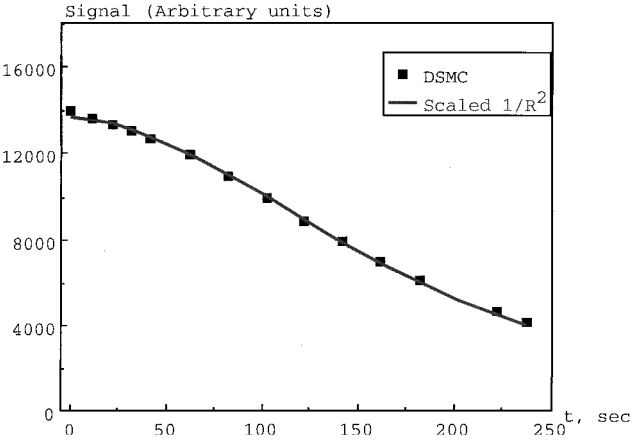

Fig. 19 Calculated time dependence of the near-field radiation signal.

the two profiles is observed, which suggests the observed induction time is related to the time for the plume to reach steady state or approximately the time needed for the plume to fill the far-field area.

To compare the time dependence of the near-field radiation with anticipated future data, the computed field of the number of radiative reactions per unit volume per unit time was integrated at different sight angles, corresponding to the mission trajectory conditions. The integration was performed over an area defined as a 21×21 pixel region surrounding the brightest pixel in the image. The area is dependent on the distance between Mir and Soyuz-TM and increased from 41×45 m at the beginning of the trajectory to 72×80 m at the end. Another factor included in the calculations was the change of the ambient density as Soyuz-TM descended from 387 to 378 km (the density increases about 10%). The results of a single DSMC calculation for the freestream conditions given in Table 1 were used for this analysis, with the radiance scaled linearly by the small changes in the freestream. The results of calculations are presented in Fig. 19 for the duration of the entire engine operation for the reentry burn. The numerically obtained time history of the near-field radiation manifests behavior very close to the profile of the scaled range function $1/R^2$, where R is the distance between Mir and Soyuz-TM. Note that a change of the internal mode contribution to the reaction probabilities does not change the $1/R^2$ dependence, and the coefficients to match the shape for $a_{\text{rot}} = a_{\text{vib}} = 0$ and $a_{\text{rot}} = a_{\text{vib}} = 1$ agree within a few percent. Likewise, if NH(A) radiation is assumed to be the plume source, it is also observed to scale as $1/R^2$.

V. Conclusions

Numerical investigations of UV radiation produced by the interaction of the plume flow from Soyuz-TM spacecraft and the ambient gas were performed for an altitude of 380 km. The DSMC method was used in the computations. To obtain grid-independent,

converged results, a sensitivity study of the method to numerical parameters was conducted. It was shown that computed radiation is sensitive to the collision cell size, whereas the impact of the number of particles, time step, and size of the computational domain is not so pronounced. It was also established that the radiation intensity is more strongly dependent on the choice of chemical model. Accounting for the internal degrees-of-freedom contribution to the reaction probability for the total collision energy model greatly reduces the radiance.

Two possible paths for water dissociation were examined, which resulted in OH formation either in the ground or excited state. The formation of OH molecules in the ground state was found to be faster by approximately a factor of two than OH(A) production along the plume axis. Because of a lower reaction threshold, ground-state OH tends to form more rapidly than OH(A) on the periphery. However, the concentration of OH(X) was found to be insignificant as a source of radiation through the collisional excitation OH(X) $\rightarrow$ OH(A). The OH(X) mole fraction of 10^{-5} in the plume was shown to be small as compared to the OH(X) production through the dissociation of water.

To examine the influence of possible radiation of excited NH as a result of dissociation of hydrazine fragments, computations were performed with both mechanisms of radiation included, from OH(A) and NH(A). It was shown that the radiation emission map for these sources is qualitatively different. Because of a considerably smaller reaction cross section and reaction threshold, the NH(A) emission occurs mainly near the nozzle exit. Whereas the maximum of radiation intensity for OH(A) is observed at about 2500 m from the nozzle exit, the maximum for NH is located less than 1500 m from the nozzle.

Because the concentration of hydrazine fragments in the plume is unknown, except that it is a trace species, a mole fraction of 10^{-5} was assumed for these fragments in the plume. Although this value is very small, if correct, the radiation from NH(A) would be two orders of magnitude smaller than from OH(A).

The results of computations were compared with available experimental data for the time dependence of the near-field radiation intensity from Soyuz-TM spacecraft, observed at the Mir space station. The computations included the factors of distance, angle of view, and altitude, affecting viewable radiation. The absolute magnitude of numerically predicted radiation is higher approximately by a factor of 5–70, depending on the chosen chemistry model for water dissociation. However, the simulations are in reasonable agreement with the near-field plume intensities. The model provides an explanation for the experimentally observed induction time of 2 s for the far-field plume data.

Acknowledgments

The work at George Washington University was supported by the Army Research Office Grant DAAG55-98-1-009 and Air Force Office of Scientific Research Grant F49620-99-1-0143 and the Ballistic Missile Defense Organization. Valuable discussions with Ingrid Wysong of the U.S. Air Force Research Laboratory are greatly appreciated.

References

[1]Karabadzhak, G. F., Plastinin, Y., Afanasiev, A., Szhenov, E., Drakes, J. A., McGregor, W. K., Nichols, J. A., Reed, R. A., Bradley, D., Teslenko, V., Shvets, N., Volkov, O., and Kukushkin, V., "Measurements of the Progress-M Main Engine Retrofiring Plume at Orbital Conditions," AIAA Paper 99-1042, Jan. 1999.

[2]Drakes, J. A., Swann, D. G., Karabadzhak, G. F., and Plastinin, Y., "DSMC Computations of the Progress-M Spacecraft Retrofiring Exhaust Plume," AIAA Paper 99-0975, Jan. 1999.

[3]Bernstein, L. S., Elgin, J. B., Pike, C. P., Knecht, D. J., Murad, E., Zehnpfennig, T. F., Galicia, G. E., and Stair, A. T., Jr., "Sources of the Infrared Radiation Generated by the Interaction of Fast O(^{3}P) with H_2O in Space," *Journal of Geophysical Research*, Vol. 101, No. A1, 1996, pp. 383–393.

[4]Levin, D., Collins, R., Candler, G., Wright, M., and Erdman, P., "Examination of OH Ultraviolet Radiation from Shock-Heated Air," *Journal of Thermophysics and Heat Transfer*, Vol. 10, No. 2, 1996, pp. 200–208.

[5]Kossi, K., Boyd, I., and Levin, D., "Direct Simulation of High Altitude Ultraviolet Emission from the Hydroxyl Radical," *Journal of Thermophysics and Heat Transfer*, Vol. 12, No. 2, 1998, p. 223.

[6]Viereck, R. A., Murad, E., Knecht, D. J., Pike, C. P., Bernstein, L. S., Elgin, J. B., and Broadfoot, A. L., "The Interaction of the Atmosphere with the Space Shuttle Thruster Plume: The NH(A-X) 336-nm Emission," *Journal of Geophysical Research,* Vol. 101, No. A3, 1996, pp. 5371–5380.

[7]Bird, G. A., *Molecular Gas Dynamics and the Direct Simulation of Gas Flows,* Clarendon, Oxford, 1994.

[8]Ivanov, M. S., Markelov, G. N., and Gimelshein, S. F., "Statistical Simulation of Reactive Rarefied Flows: Numerical Approach and Applications," AIAA Paper 98-2669, June 1998.

[9]Bird, G. A., "Monte-Carlo Simulation in an Engineering Context," *Rarefied Gas Dynamics,* edited by S. Fisher, Vol. 74, Progress in Astronautics and Aeronautics, AIAA, New York, 1981, pp. 239–255.

[10]Borgnakke, C., and Larsen, P. S., "Statistical Collision Model for Monte Carlo Simulation of Polyatomic Gas Mixture," *Journal of Computational Physics*, Vol. 18, No. 4, 1975, pp. 405–420.

[11]Ivanov, M. S., "Transitional Regime Aerodynamics and Real Gas Effects," *Proceedings of the International Symposium on Aerospace and Fluid Science*, 1993, pp. 77–101.

[12]Bird, G. A., "Simulation of Multi-Dimensional and Chemically Reacting Flows," *Proceedings of the 11th International Symposium on Rarefied Gas Dynamics*, edited by R. Campargue, Commissariat a l'Energie Atomique, Paris, 1979, pp. 365–388.

[13]Kofsky, I. L., "Excitation and Diagnostics of Optical Contamination in the Spacecraft Environment," U.S. Air Force Geophysical Lab., AFGL-TR-88-0393, July 1988.

[14]Baulch, D. L., Drysdale, D. D., Home, D. G., and Lloyd, A. C., *Evaluated Kinetic Data for High Temperature Reactions, 1. Homogeneous Gas Phase Reactions of the H_2-O_2 System*, Butterworths, London, 1972.

[15]Orient, O. J., Chutjian, A., and Murad, E., "Observation of CH $A \rightarrow X$, CN $B \rightarrow X$, and NH $A \rightarrow X$ Emissions in Gas-Phase Collisions of Fast O(^3P) Atoms with Hydrazines," *Journal of Chemical Physics*, Vol. 101, No. 10, 1994, pp. 8297–8301.

J. P. Gore
Associate Editor